Seismicity, seismotectonics and crustal velocity structure of the Messina Strait (Italy)

Luciano Scarfì, Horst Langer, and Antonio Scaltrito

Istituto Nazionale di Geofisica e Vulcanologia, sezione di Catania, Piazza Roma, 2, 95123 Catania, Italy

Abstract

The Messina Strait is the most important structural element interrupting the southernmost part of the Alpine-Apenninic orogenic belt, known as the Calabro-Peloritan Arc. It is being a narrow fan-shaped basin linking the Ionian Sea to the Tyrrhenian Sea. This region is affected by considerable seismic activity which mirrors the geodynamic processes due to the convergence between the African and the Eurasian plates. In the last four centuries, a significant number of disastrous earthquakes originated along the Arc. Among these, the most noteworthy event occurred on December 28, 1908 (known as the Reggio Calabria-Messina earthquake), in the Messina Strait area and caused a large tsunami and more than 100,000 casualties. In this research we focus on the relationships between the general tectonic setting, which characterize the Messina Strait and adjacent areas, seismicity patterns and the crustal structure. We analyzed a data set consisting of more than 300 events occurring in the years from 1999 to 2007, having a magnitude range from 1.0 to 3.8. This data set was exploited in a local earthquake tomography, by carrying out a simultaneous inversion of both the three-dimensional velocity structure and the distribution of seismic foci. We applied the "tomoADD" algorithm, which uses a combination of absolute and differential arrival times and a concept of self-adapting grid geometry, accounting for ray density encountered across the volume. With this method the accuracy of event locations is improved and velocity structure near the source region is resolved in more detail than standard tomography.

Fault plane solutions were obtained for the major and best-recorded earthquakes. The obtained velocity images highlight vertical and lateral heterogeneities that can be associated with structural features striking from NNE-SSW to NE-SW. These results are consistent with important tectonic elements visible at the surface and the pattern delineated by earthquake locations and focal mechanisms.

Keywords: Crustal structure, Focal mechanism, Seismicity, Seismotectonics, Tomography

1. Introduction

A hundred years have now passed since the disastrous earthquake on December 28, 1908, one of the largest events ever recorded in the central Mediterranean (Boschi et al., 2000), destroyed Messina, Reggio Calabria and the adjacent areas. In addition to the damage due to the impact of the seismic waves, much destruction and loss of life was caused by a tsunami which developed as a consequence of the earthquake.

The Messina Strait is without doubt the most important structural element interrupting the southernmost part of the Alpine-Apenninic orogenic belt, known as the Calabro-Peloritan Arc. (Fig. 1). It forms a branch of the Ionian Sea separating SW Calabria from NE Sicily. Its western margin belongs to an escarpment that stretches over 70 km from Messina towards the Mt. Etna area. In W - E direction, the elevation falls from about 1000 a.s.l. to a depth of more than 1000 b.s.l. in the center of the Strait, which means a total elevation difference of 2000 m along a distance of less than 20 km. The considerable orographical differences in NE Sicily, SW Calabria and in the Ionian Sea are the expression of intense tectonic activity. Indeed, from a seismotectonic point of view, the Calabro-Peloritan Arc region is characterized by considerable geodynamic instability (Gasparini et al., 1982; Monaco and Tortorici, 2000; CPTI work group, 2004). In the last four centuries, a considerable number of violent earthquakes, with epicentral intensities of 10 to 11 degrees MCS (CFTI-Med 4.0), have occurred along the sector of the Arc stretching from the Gulf of S. Eufemia to the Nebrodi Mountains. A significant aspect of this activity is the devastating impact produced on the ground: massive landslides that narrow and sometimes obstruct valleys, the formation of small lakes, the deviation of watercourses, slumps, and the fracturing and liquefaction of soil (Bottari et al., 1986; Murphy, 1995; Galli, 2000; Tertulliani and Cucci, 2008). These dramatic phenomena of ground failure are generally considered indicative of the shallow depth of the earthquake source. Indeed, analyses of the macro-seismic fields of the best-documented events favor the hypothesis of a position of the sources – or part of them - close to the surface (see, e.g. Bottari et al, 1986). However, the lack of surface faulting after the largest shocks makes the understanding of the source location as well as the geometry of the fault system a difficult task. We have no ground proof as to whether the important topographical elements around the Messina Strait form true fault systems, perhaps cutting the entire crust and reaching the upper mantle. The identification of such fault systems is further hindered by the great depth of the Ionian Sea (more than 1000 m in the southern part of the Messina Strait) - clearly, there are difficulties in recognising geological formations and tectonic structures underlying the juvenile sediments covering the sea floor at such depths. As a consequence, the dislocation nature of the 1908 Messina Strait earthquake has been a matter of debate (see web site of DISS). Ghisetti (1984) has suggested a graben-like style of faulting for the Messina Strait. For other authors (e.g. Valensise and Pantosti, 1992), the fault causing the 1908

Messina Strait earthquake is seen as a low angle, blindly ending element dipping east, rather than a steeply westward dipping structure parallel to the northeastern coast of Sicily (e.g. Bottari et al., 1986).

Research efforts by various institutions have enabled collecting a sizeable set of seismic records, disclosing the possibility of an in-depth investigation of seismotectonic patterns in the area. In particular, the Istituto Nazionale di Geofisica e Vulcanologia has been running a permanent local seismic network from 2001 on; before this time the network was operated by the "Sistema POSEIDON" since the middle of the 1990's. In a recent paper, Barberi et al. (2004) investigated the 3D velocity structure on a fairly wide scale (40 km horizontal grid spacing and 10 km in vertical direction) in an area covering the Southern Tyrrhenian Sea and the Calabrian Arc region. In this investigation, a positive velocity anomaly was found in the Messina Strait at a depth of about 15 km. A further feature of interest here is a negative anomaly stretching from the area north of Mt Etna in ENE direction into the Ionian Sea and the southern tip of the Italian peninsula.

In this research, we focus on the relationship between the general tectonic setting, which characterizes the Messina Strait and adjacent areas, seismicity patterns and the crustal structure. We used a data set consisting of a total of 360 events with a magnitude range from 1.0 to 3.8 occurring in the period from 1999 to 2007. This data set is exploited in a local earthquake tomography (LET), by carrying out a simultaneous inversion of both the three-dimensional velocity structure and the distribution of seismic foci.

In conventional LET (e.g. using the SimulPS12 code; see Evans et al., 1994) the inversion of velocity parameters and earthquake location is carried out on the basis of absolute arrival time readings. These locations are affected by errors collected over the whole ray path, hence the risk that velocity perturbations outside the well illuminated area are mapped into it. Furthermore, the use of absolute arrival times typically requires the definition of station corrections in order to minimize site effects. One way round this dilemma is to use differential travel times, as proposed for instance by Waldhauser and Ellsworth (2000). For earthquake clusters, with foci lying close to each other, travel time errors due to incorrect velocity models in the volume outside the cluster will essentially cancel out. As a consequence of using relative travel times, the use of station corrections becomes obsolete. At the same time, it can be shown (see e.g. Waldhauser and Ellsworth, 2000; Menke and Schaff, 2004) that the use of differential travel times considerably improves the relative locations and provides at least the same quality of absolute hypocenter locations as do standard location techniques. Conventional LET uses a velocity grid defined in Cartesian coordinates and with a regular cell or grid spacing to be defined a priori. The advantage of working with fixed cells lies in its simplicity. For instance, such velocity grids can easily be used in Monte Carlo experiments (see Raffaele et al., 2006) in order to examine the statistical stability of the results. However, the ray distribution is typically highly uneven due to non-uniform station configuration, the distribution of hypocenters and ray bending. The regular grid geometry makes it difficult to adapt to

the unevenness of the rays with the outcome that some cells may have few or no rays, while others may have a very high ray density sampling. Ideally, the inversion grid should be distributed adaptively to match the resolving power of the data (see Zhang and Thurber, 2005).

Zhang and Thurber (2003, 2005) developed computer codes which allow to bypass the problems encountered with absolute hypocenter locations and inflexible velocity grids. Here, we have been using their code tomoADD. Both absolute and relative arrival time readings can be used. The accuracy of the latter can be improved for multiplet events, where relative arrival times can be obtained using correlation and coherency based techniques, such as the cross-spectral method. In the adaptive generation of the velocity grid, new grid points are inserted in a tetrahedron of former grid points if a certain threshold value of weighted ray density (DWS) is reached. At the same time, older grid points may be removed if their DWS falls below a limiting value. For more details, see Zhang and Thurber (2005).

Finally, our preference for TomoADD was justified from a comparison of the overall RMS travel time residuals obtained with the classical LET method (Evans et al., 1994). TomoADD gave considerably lower residuals (0.13 s) than classical LET using the SimulPS12 code, where an overall residual of 0.29 s was encountered.

2. Tectonic Setting

The investigated area belongs to the Calabro-Peloritan Arc, which is part of the Apennine-Maghrebian orogenic belt along the Africa-Europe plate boundary. In this sector, convergence processes, from the Neogene-Quaternary on, led to the formation of three distinct tectonic domains: i) the Tyrrhenian back-arc basin (extensional domain), ii) the Alpine-Apenninic orogenic belt (domain of crust shortening) and iii) the Hyblean Foreland (Fig. 1). The Calabro-Peloritan Arc connects the NW-SE-trending southern Apennines with the WSW-striking Maghrebian thrust zones (Fig. 1). Its recent geodynamic evolution has been closely related to the opening of the Tyrrhenian Sea beginning in the middle Miocene, the ESE-ward drift of the Calabro-Peloritan massif and the subduction of Ionian oceanic lithosphere underneath Calabria (Finetti and Del Ben, 1986). Several, often contrasting hypotheses, have been proposed for the current geodynamic of the area, such as active subduction beneath the southern Tyrrhenian Sea (Barberi et al., 1973), or rifting dominated by slab sinking and passive subduction (Finetti and Del Ben, 1986; Patacca et al., 1990). Debate on the most appropriate model is still open. However, the presence of a subducted slab is marked by the occurrence of intermediate and deep earthquakes (between 50 and 400 km) beneath the southern Tyrrhenian Sea, along a NW-dipping Benioff zone (Gasparini et al., 1982; Anderson and Jackson, 1987; Giardini and Velonà, 1991), and by a seismic high-velocity anomaly in the mantle (e.g. Selvaggi and Chiarabba, 1995).

The Messina Strait is the most important structural discontinuity cutting the southern part of the Arc, forming a narrow fan-shaped basin linking the Ionian Sea to the Tyrrhenian Sea. Following Ghisetti (1992), it is bounded by high angle normal faults with prevailing N-S to NE-SW orientation, and identified as active during Pliocene and Pleistocene times. Among the major faults, the Larderia-Curcuraci fault system bounds the eastern margin of Sicily. The Reggio Calabria-Calanna-S. Eufemia and the Armo-Delianuova fault systems are situated on the Calabrian side of the Strait. Other NW-SE and E-W striking fault families contribute to a rather complex structural picture, particularly in Calabria (Fig. 1). Consequently, long-term evolution and the structural setting of the Strait are still a matter of discussion (see among others: Valensise and Pantosti, 1992; Tortorici et al., 1995).

Seismological, geodetic and structural data demonstrate that the studied area is characterized by active extensional tectonics, at least in the upper part of the crust between depth from surface to 15 km. Indeed, several authors (Tortorici et al., 1995; D'Agostino e Selvaggi, 2004; Neri et al., 2004) claim two different styles of deformation accommodating the Europa-Africa convergence in Sicily and in the Calabro-Peloritan Arc. In their opinion the area to the west of the Aeolian-Tindari-Giardini lineament (ATG) is dominated by a compressional regime presumably induced by plates convergence. The area to the east of the lineament is characterized by NW-SE extension that may be related to an Ionian subduction slab rollback.

3. Data Set and Seismicity

We analyzed seismicity in the area of the Messina Strait by using the data recorded the local network operated by the "Sistema POSEIDON" and subsequently by Istituto Nazionale di Geofisica e Vulcanologia in eastern Sicily and southern Calabria since the 1990's (Fig. 1b). The network consists of three-component stations. Since 2004, stations with analogical telemetry have been upgraded with modern digital VSAT based data transmission and equipped with three-component broadband sensors (40 s). In order to reduce the azimuth gap, the stations of the nearby Aeolian Islands, Mt. Etna and of the National permanent seismic networks are occasionally included as they provide additional onset readings for the most energetic events. All the stations use the same base time, set by GPS time.

In the area extending from 37.81° N to 38.33° N, and 15.35° E to 16.01° E, about 360 earthquakes (Fig. 2) were recorded between 1999 and 2007. In the hypocenter distribution, with coordinates taken from INGV-CT catalogue (see http://www.ct.ingv.it/Sismologia/analisti/default.asp), we recognize a concentration of foci within the uppermost 15-20 km. A similar limitation of focal depth in the Peloritani Mountains has been explained by Langer et al. (2007) in terms of a "Brace-Goetze Lithosphere", where rock rheology is assumed to depend on depth and temperature (for more details on this subject see also Stüwe, 2002). Greater depth encountered in the south may be related to the presence of the

subducted slab, but this must be read with caution as location uncertainties increase due to the unfavorable network configuration. Most of the earthquakes are located within three zones: i) in southwestern Calabria (inland), ii) in the Strait between Messina and Reggio Calabria and iii) in the Ionian Sea, west of Cape S. Alessio. On the other hand, very few events were located in the inland area, between Cape S. Alessio and the northeastern tip of Sicily.

For our investigation, we filtered the original data set according to quality criteria of location. In particular, we selected only well located events, i. e. those with at least 9 observations (P- and S-phases), root-mean-square (RMS) residuals smaller than 0.35 s and horizontal and vertical location errors lower than 2.5 km and 3.5 km, respectively. We also tested the location stability - using the tomoADD code but keeping the velocity parameters fixed - by shifting the trial hypocenters randomly in the space (see Husen et al., 1999). This helped identify events for which different locations with equivalent travel-time residuals can be found. Note that the presence of events with unstable locations bears the risk of introducing biases as the inversion process may decrease the travel-time residuals by shifting around the hypocenter coordinates instead of adjusting the velocity model parameters properly. In practice, we have compared the locations with unperturbed starting solutions and the locations with starting solutions to which a random perturbation of up to ±8 km was added. We repeated the test five times and considered the realisations where the difference between the solutions were maximum. In doing so, we have a conservative estimate of the stability of the hypocenter locations by removing events with horizontal or vertical location variations greater than 3 km. All tests revealed fairly stable epicenter determinations for almost all the events. In fact, the differences of the results with non-perturbed starting locations and results with randomly perturbed ones was fairly low (1 km or less for 96% of the well locatable events matching the quality criteria mentioned above). Finally, we obtained a data set of 244 well locatable and stable events which were used in the simultaneous inversion of both the velocity structure and the hypocenter location.

4. 3D Imaging

A total of 1785 P and 1163 S absolute arrival times and about 46250 catalogue-derived differential times were jointly inverted using the tomoADD algorithm (Zhang and Thurber, 2005) for hypocentral parameters and velocity structure.

For the given amount of S-wave data available, however, we limit ourselves to discuss the velocity model for P-waves and address to further studies with an enriched data set, when in particular more S-wave arrival times will be available. We decided to reduce the weight of S-wave arrivals to 20% for fitting the velocity model, whereas their full weight is maintained for the hypocenter location. In doing so, we avoid that S-wave velocities, which are less constrained than those for P-waves, are shifted around artificially reducing the overall residuals.

We started the inversion from a regular horizontal grid, with 5x5 km node spacing covering an area of 60x60 km, based on the P and S ray paths of the selected data obtained by the pseudo-bending method (Um and Thurber, 1987) (Fig. 3). Vertical grid spacing varies between 2 and 6 km and covers a depth range from the surface to 33 km depth, following the 1D reference velocity model (Langer et al., 2007). Higher weighting was applied first to the catalogue absolute data in order to obtain a large-scale result. Then, higher weights were assigned to the differential data to refine the event locations and the velocity structure near the source region. The damping values were selected on the basis of L-curves of solution and data variances (see Zhang and Thurber, 2005).

The number and position of inversion mesh nodes change from one iteration to the next as the method automatically adjusts the inversion mesh nodes according to the data distribution. The procedure implemented in TomoADD is based on the construction of tetrahedral and Voronoi diagrams and the use of the Qhull algorithm (see Zhang and Thurber, 2005). In this way, the density of the inversion mesh nodes is higher in volumes where more rays are passing. The strategy applied in tomoADD for the design of the mesh is based on the derivative weight sum (DWS), which quantifies the ray density around each model node. DWS is a key parameter for understanding how well the model is resolved (Haslinger et al., 1999). Moreover, the adaptive mesh method considers the different ray distribution between the P and S waves. At the end of the iterative process, the inversion mesh nodes for P and S waves are irregularly distributed, accounting for the heterogeneous distribution of the rays (Fig. 4). As a result, ray sampling for each inversion mesh node is more uniform and the tomographic system proves more stable than in a conventional grid with regular spacing (e.g. Zhang and Thurber, 2005).

In Fig. 5, we compare the distribution of the DWS for a conventional regular mesh created with tomoDD and the one obtained with tomoADD. In the latter, we notice 1379 nodes with non-zero DWS values, all having DWS values greater than 100. The average DWS value is 390 with standard deviation 133. With regular inversion grid (tomoDD), there are 1359 nodes with non-zero DWS value, among which only 36% of them have DWS values greater than 100. Many inversion grid nodes have DWS values less than 10 and the average DWS value is 286. In other words, the adaptive strategy of mesh creation in tomoADD exploits the available information efficiently, whereas the regular grid yields a highly uneven DWS distribution, which becomes a critical issue when only a limited amount of data is available.

Fig. 6 shows the three dimensional velocity structure for P-wave velocities in the Messina Strait area. We have marked the zones with a reasonable illumination (DWS > 100) with a yellow line. The shallowest layers, at a depth of 6 and 8 km, are characterized by strong positive anomalies in the northern part of the Messina Strait, as well as in the area of the Mts Peloritani and the Mt. Aspromonte. Positive P-wave anomalies are also found more southward along the eastern coast of Sicily, in particular in the offshore area of the Cape S. Alessio. A negative anomaly occurs on the Calabrian side, in an area lying more or less between the Reggio Calabria-Calanna-S. Eufermia and the Armo-Delianuova fault

systems. A similar picture is found at a depth of 10 km, with higher P-wave velocities from north, in the Strait, southward, along the eastern coast of Sicily, interrupted by lower velocity zones with trends cutting the coastline. Again, we notice relatively high P-velocities in the Mts Peloritani and in the Mt. Aspromonte. A negative anomaly is clearly visible in a northeast-southwest striking stripe from the southern part of the Strait to the fault systems of the Calabrian side. At deeper layers (12 and 15 km depth) we notice a slightly modified picture. In fact, in the central and southern parts of the studied area, we notice two zones of low P-wave velocities, trending about ENE-WSW, separated by a ridge with high P-wave velocities. At a depth of 18 km the aforementioned structures are still identifiable, though the picture is blurred by the worsening illumination at this depth. Cross-sections of V_P are displayed in Fig. 7.

5. Stability Analysis with Monte Carlo Tests

Monte-Carlo tests are popular instruments in parameter studies, used to check the stability of forward and inverse modeling. They have the advantage of making very limited a-priori assumptions about possible errors. However, they entail an additional computational burden as the inversions have to be repeated a number of times. This additional effort becomes affordable with increasing computer capacities. During the Monte Carlo tests, we have added uniformly distributed random disturbances to our input data, i.e. the arrival times and the starting velocity model. In particular, uncertainties of the arrival time readings were accounted for by adding a random perturbation of up to ±50 ms for first onset readings and up to ±100 ms for S-phase arrival times. The starting velocity model has been examined in detail by Langer et al. (2007) and was found to be the best available one. Nonetheless, as its parameters make up part of the input information we examined the effect of possible uncertainties. We applied random perturbations in the range of ± 0.l km/s both for the P- and S-wave velocities. We repeated the Monte Carlo test 15 times in order to achieve a reasonable significance. Focusing on grid nodes with DWS of at least 100, we found 50 percent of all nodes (i. e. nodes between the 25 % and 75% quartiles) scatter in the range of ± 110 m/s around the results without random perturbation. The standard deviations for the velocity models give a range of ± 130 m/s.

The travel time residuals are the measure of the goodness of fit for the inverted model. A comparison of residuals obtained with and without randomization helps understand whether the assumed uncertainties of input data are realistic or overestimated. In the first case, we expect that travel time residuals obtained with randomization are equivalent to those without, as the accuracy of input data is essentially unaltered. In the second case, we expect that the quality of inverted models worsens significantly. In our case, all inversions carried out with perturbed input data gave slightly higher travel time residuals (about 10% for both absolute and weighted) than the inversion carried out without randomization. We thus conclude that the assumed uncertainties, with respect to arrival time readings and initial guess

of the velocity model, are on the safe side as the random perturbation applied to the input data tends to overestimate the true inaccuracy of input parameters. This implies that the expected scatter of the inverted velocity parameters, as far as being caused by the uncertainty of the input parameters, also represents a conservative estimate. On the other hand, we may consider these values a measure of lower threshold for distinguishable anomalies. Velocity differences in the tomographic image which are of the order of 100 to 130 m/s might merely be an effect of an uncertainty of arrival time picking or the parameters of the initial velocity model.

6. Synthetic Testing

Overall, travel time residuals, DWS and other parameters furnish first-order diagnostics for the assessment of the resolution, whose real significance depends on the individual conditions of the inversion problem and whose understanding needs intuition. We therefore carried out numerical experiments with synthetic models, which give an immediate and straightforward idea of the inversion stability, potentially insignificant or artificial features and the sensitivity with respect to the choice of the starting model. Here, we have used synthetic travel times calculated for typical test models. These data were then inverted using the same starting model, choice of parameters and control values as for the real data.

One type of synthetic test to assess the structural resolving power is the restoring resolution test (Zhao et al., 1992). It consists of calculating the synthetic travel times for both the velocity model and hypocenter locations obtained through the inversion. Additionally, noise is added to both travel times and initial guesses. By comparing the results of the inversion of synthetic travel times with those obtained with the real data, we can estimate the restoring capacity of the data set. A major problem of such a restoring resolution test may be local minima in areas of low resolution, leading to the impression of good resolution in actually unresolved areas. The use of a characteristic model avoids this difficulty (Haslinger et al., 1999). A characteristic model contains the size and the amplitude of anomalies seen in the inversion results, but with different sign of the amplitude. It is highly unlikely that such a model will represent the same mathematical minimum as the one obtained with the real data. Therefore, areas of low resolution will be indicated by not restoring the characteristic model.

We performed both synthetic tests. Following the strategy of the characteristic model (see Haslinger et al., 1999), we designed a velocity model with anomalies at the same position as the ones encountered from the original model but of opposite sign; i. e. positive anomalies become negative, negative become positive. The absolute deviations are maintained. As in our original inversion we started with the optimum 1D model proposed by Langer et al. (2007) and applied TomoADD to the synthetic travel times. In the characteristic test we noted that the position and sign of the

velocity anomalies are recovered fairly well, at least for nodes where DWS was higher than 100. However, the amount of anomalies is considerably smaller, with a model variance underestimating the true one (Fig. 8a). Travel time residuals for the inverted test model were about 30 ms.

With the restoration test we followed a similar strategy to that applied by Scarfi et al (2007). We calculated synthetic travel times for the inverted velocity structure and hypocenter locations. Subsequently, we applied a random perturbation to travel time. Carrying out the inversion without applying random perturbation to the input parameters we achieved a similar travel time residual as with the characteristic model, i. e. 30 ms. Again, the inverted anomalies are similar to the a-priori ones, with respect to position and sign (Fig. 8b). On the other hand, their amount was found smaller than the a-priori values, leading to smaller model variance. With noisy input parameters (perturbations taken from the Monte Carlo experiments, with up to ±50 ms for P-wave onsets, ±100 ms for S-phase picking) the travel time residuals increase to about 50 ms. The residuals reach 100 ms, when an additional systematic error of up to 0.2, representing for instance station corrections, is assumed. The overall characteristic of results is the same as before, in the sense that inverted and a-priori anomalies match both with respect to their position and sign, whereas the inverted model tends to be considerably smoother than the a-priori one.

7. 3D Location

Besides the velocity model, seismic tomography also introduces modifications of the hypocenter location. Compared to the original locations our revised ones show a major degree of clustering (e.g. see the clusters marked with S1 and S2 in Fig. 9). This is no surprise since tomoADD – similar to HypoDD - is based on travel time differences between the events and a major clustering of hypocenters has already been noted in the literature when travel time differences between event clusters are used instead of single absolute arrival time readings (see, e.g, Waldhauser and Ellsworth, 2000; Scarfì et al., 2005). In our final locations obtained with tomoADD (Fig. 9), we recognize epicenters nicely aligned along the Reggio Calabria-Calanna-S. Eufemia and the Armo-Delianuova fault systems. A further linear alignment of epicenters, striking in a NW direction is found offshore Cape Taormina.

The clusters of events marked as S1 and S2 form two families of multplet events with very similar waveforms, which can be exploited for high precision relative location analysis. We examined the geometry of the two families in more detail using high precision relative location with the master-event technique (e.g. Scarfì et al., 2005) and performed a Principal Component Analysis (PCA) on the covariance matrix of the relative hypocenter locations (see Figs. 10a and 10b). For S2, taking the eigenvalues and corresponding eigenvectors, we infer a cluster forming a N 30° E striking planar element with a dip of 70° W. From the square root of the largest eigenvalue and its eigenvector we obtain a

hypocenter cloud elongated about 1100 m (68% value, in terms of confidence given by ± one standard deviation) in a more or less horizontal direction. Using the same technique, for the S1 cluster, we found a major elongation in a N 20° W striking direction and a dip of about 80° E. We estimate an extension of the data cloud corresponding to about 360 m. In both S1 and S2 clusters, the smallest extension, measured perpendicular the plane spanned by the two major eigenvectors, is of the order of 140 m. This is close to the possible uncertainty of relative location due to intrinsic inaccuracy of travel time determination (see Scarfi et al., 2005).

8. Fault Plane Solutions and Tectonic Structures.

Fault plane solutions were obtained for the major and best recorded earthquakes occurring in the years 1999-2007. The solutions are based on first arrival P-wave polarities. The nodal lines were identified using the code published by Reasenberg and Oppenheimer (1985). On the basis of the fault plane solutions and considering patterns inferred from event locations, we may distinguish four seismotectonic regimes: (i) the Messina Strait, (ii) the Mt. Aspromonte, (iii) the Ionian Sea adjacent to the southernmost coast of Calabria, (iv) the offshore region of Cape Taormina and Cape S. Alessio (see Fig. 11).

The Messina Strait area is characterized by normal faulting events along NE to NNE striking planes, with almost vertical P-axes, and T-axes striking WNW-ESE. Similar patterns were reported by Scarfi et al. (2005) and Giammanco et al. (2008) for the nearby Peloritani Mountains area in northeastern Sicily (see also Fig. 11). The orientation of the nodal planes is also consistent with the orientation of the S2 cluster as well as the earlier mentioned epicenter alignments in Calabria. In the Mt. Aspromonte normal faulting as well as strike slip solutions were found, with vertical P-axes or horizontal P-axes striking NNE. In the figure, it can be seen that nodal planes follow trends of tectonic structures visible at the surface. In the Ionian Sea close to the southernmost coast of Calabria the earthquakes show a prevailing normal faulting mechanism with a minor strike slip component, and an extension in NE direction. In the offshore area of Cape Taormina and Cape S. Alessio, there are two events with clear strike slip movement and two normal faults with T-axes oriented WNW-ESE.

9. Discussion and conclusions

In this paper we have investigated the three dimensional velocity structure in the Messina Strait area. In this context, we re-evaluated the seismicity patterns by relating them to fault plane solutions and tectonic evidences visible at the surface. Seismic tomography was carried out using the recently developed code tomoADD (Zhang and Thurber, 2005),

334 which gave the best arrival time residuals compared to the more classical codes SimulPS12. TomoADD uses absolute
335 arrival times as well arrival time differences among earthquake clusters, and applies a flexible concept of mesh
336 generation. Compared to conventional local earthquake tomography, tomoADD gives at least the same accuracy of
337 earthquake location and guarantees a more homogeneous illumination of the grid cells. The inversion thus makes a
338 more efficient use of the available data set and improves the reliability of results.
339 We have assessed the stability of our inverted model with respect to uncertainties of the input parameters by applying a
340 Monte Carlo test. We also analyzed the resolution capabilities of the data set, in particular using the DWS distribution
341 and performing synthetic tests. We found that the velocity structure is well resolved at least for nodes where DWS was
342 equal/higher than 100. This condition is met in layers with depth ranging from 6 km to 18 km. From synthetic tests we
343 infer, that the position and sign of velocity anomalies can be recovered fairly well, however, underestimating the
344 variance of the velocity model. In this light our results are understood as a smooth, i. e., conservative estimate of the
345 true heterogeneity of the structure of the crust.
346 A major point for discussion concerns the structural setting of the Messina Straits and thus the geometry of the
347 seismogenic faults. From the pattern of high- and low-velocity anomalies visible in the layers at different depths as well
348 as in the cross-sections (Figs 6 and 7), we identify a NE-SW striking stripe with negative velocity anomalies. On the
349 Calabrian mainland, this stripe essentially coincides with the zone delimited by the Reggio Calabria – Calanna - S
350 Eufemia (northern border) and Armo - Delianuova faults (southern border, see Fig. 7, cross-sections A-A'', B-B", C-C"
351 and also F-F"). The continuation of this trend in the Ionian Sea can be readily identified in the southernmost profiles,
352 closer to the NE-Sicily coast. Clear positive P-wave velocity anomalies are found in the northern part of the Messina
353 Strait and along the eastern coast of Sicily. The positive anomaly in the Peloritani Mountains is separated from the one
354 of the Strait by a narrow but evident stripe of relatively low velocities. In the deeper layers (12, 15 and 18 km) we
355 notice a ridge of positive anomalies starting in the area of Cape Taormina, then bending in an ENE direction. The ridge
356 crosses the Ionian Sea and is also found in Calabria. For the sake of clarity, figure 12 shows the topography of the 6.5
357 km/s V_P isosurface which summarizes the main features of the obtained velocity structure. In the figure, we also plot the
358 epicenter of the earthquakes located above the isosurface.
359 Our locations were carried out for a revised data set, focusing on earthquakes satisfying specific quality criteria with
360 respect to the number of available arrival time readings, stability of the starting solution for the hypocenter location, and
361 the goodness of fit (residual). The critical selection of events is necessary in order not to bias the inversion, but also to
362 avoid artifacts, which could be erroneously interpreted as seismotectonic patterns (see Scarfì et al., 2003, 2005).
363 Seismic foci are mainly located on the boundaries of high/low velocity regions (Figs 6, 7 and 12), with a characteristic
364 depth between 5 and 15 km. The distribution of well located hypocenters reveals a number of patterns related to

structures inferred from other evidences. Among others we note foci accompanying the Armo – Delianuova as well as the Reggio Calabria fault lineaments. Other event locations are found along alignments parallel to the eastern coast of Sicily. High precision relocation of the multiplet family S2 revealed a similar trend, furnishing further evidence for the presence of a NNE striking element. In the southern part of the investigated area, there is an increase of focal depth up to 40 km for the events south of the Calabrian coast (Fig. 9). Here, a rather irregular distribution of hypocenters makes it difficult to identify underlying tectonic structures. On the other hand, the mapping of geological structures is hindered by the sea cover, reaching depths of over 1000 m in the studied area.

Concerning fault plane solutions, earthquakes located in the Messina Strait, the Peloritani Mountains (Scarfì et al., 2005) and adjacent areas on the Calabrian land side reveal a normal faulting mechanism along NNE or NE striking planes, which is consistent with the overall regional trends of tectonic motion, i. e. extension in WNW-ESE direction. Strike slip mechanism was found for two events located offshore Cape Taormina, but again with P-axis striking NNE. The focal mechanisms of earthquakes falling in the Ionian Sea, south of the Calabrian coast, reveal a change of the stress field as P-axes striking in NW direction prevail.

In conclusion, the various seismological features – 3D velocity structure, seismicity patterns, fault plane solutions - confirm that important tectonic elements visible at the surface reach a considerable depth, at least down to the levels illuminated by earthquake activity. The graben-like structure is well identifiable in the calabrian inland and continues underneath the Messina Strait. The northeastern coastline of Sicily from Taormina to Messina is accompanied by considerable velocity contrasts well identifiable down to a depth of 12 to 15 km. The Messina Strait as well as the adjacent Perloritani Mountains are characterized by extension perpendicular to the NNE striking elements. Both hypocenter locations and focal mechanisms suggest that seismotectonic characteristics in the southern part differ from the picture found in the Messina Strait and adjacent zones. In particular, focal depths of the events increase and the principal direction of major horizontal stress turns from NNE to NW.

Acknowledgments

We wish to thank H. Zhang for allowing us to use the code TomoADD, our colleagues P. De Gori and A. Amato at INGV-CNT for providing data from National seismic network and two anonymous reviewers for carefully reading the manuscript and their constructive criticism. Helpful suggestions by the editor, George Helffrich, are also highly appreciated.

References

Anderson, H., and Jackson, J., 1987. The deep seismicity of the Tyrrhenian Sea. Geophys. J. R. Astr. Soc. 91, 613-637.

Barberi, F., Gasparini, P., Innocenti, F., Villari, L., 1973. Volcanism of the Southern Tyrrhenian Sea and its geodynamic implications. J. Geophys. Res. 78, 5221-5232.

Barberi, G., Cosentino, M.T., Gervasi, A., Guerra, I., Neri, G., Orecchio, B., 2004. Crustal seismic tomography in the Calabrian Arcregion, south Italy. Phys. Earth Planet. Inter. 147, 297-314.

Boschi, E., Guidoboni, E., Ferrari, G., Mariotti, D., Valensise, G., 2000. Catalogue of strong Italian earthquakes, Ann. Geofis. 43, 268.

Bottari, A., Carapezza, E., Carapezza, M., Carveni, P., Cefali, F., Lo Giudice, E., Pandolfo, C., 1986. The 1908 Messina Strait earthquake in the regional geostructural frame work. J. Geodyn., 5, 275-302.

CFTI-Med 4.0, Guidoboni, E., Ferrari, G., Mariotti, D., Comastri, A., Tarabusi, G., Valensise, G. Catalogue of strong earthquakes in Italy 461 B.C. – 1997 and Mediterranean area 760 B.C. – 1500. An advanced Laboratory of historical seismology, http://storing.ingv.it/cfti4med/.

CPTI Work Group, 2004. Catalogo Parametrico dei Terremoti Italiani, versione 2004 (CPTI04). INGV, Bologna, http://emidius.mi.ingv.it/CPTI04/.

DISS Working Group, 2005. Database of Individual Seismogenic Sources (DISS), Version 3.0.1: a compilation of potential sources for earthquakes larger than M 5.5 in Italy and surrounding areas. INGV, Roma, http://diss.rm.ingv.it/diss/

D'Agostino, N., and Selvaggi, G., 2004. Crustal motion along the Eurasia-Nubia plate boundary in the Calabrian Arc and Sicily and active extension in the Messina Straits from GPS measurements. J. Geophys. Res. 109, B11402, doi:10.1029/2004JB002998.

Evans, J.R., Eberhart-Phillips, D., Thurber, C.H., 1994. User's manual for simulps12 for imaging Vp and Vp/Vs: a derivative of the "Thurber" tomographic inversion simul3 for local earthquakes and explosions. USGS Open-file Report, pp. 94–431.

Finetti, I., and Del Ben, A., 1986. Geophysical study of the Tyrrhenian opening. Boll. Geof. Teor. Appl. 110, 75-155.

Galli, P., 2000. New empirical relationships between magnitude and distance for liquefaction, Tectonophysics 324, 169-187.

Gasparini, C., Iannaccone, G., Scandone, P., Scarpa, R., 1982. Seismotectonics of the Calabrian Arc. Tectonophysics 84, 267-286.

Ghisetti, F., 1984. Recent deformations and the seismogenic source in the Messina Strait (Southern Italy). Tectonophysics 210, 117-133.

Ghisetti, F., 1992. Fault parameters in the Messina Strait (southern Italy) and relations with the seismogenic source. Tectonophysics 210, 117-133.

Giammanco, S., Palano M., Scaltrito A., Scarfì L., Sortino F., 2008. Possible role of fluid 461 overpressure in the generation of earthquake swarms in active tectonic areas: The case of 462 the Peloritani Mts. (Sicily, Italy). J. Volc. Geoth. Res., 178, 795-806, doi: 463 10.1016/j.jvolgeores.2008.09.005.

Giardini, D., and Velonà, M., 1991. The deep seismicity of the Tyrrhenian Sea. Terra Nova 3, 57-64.

Haslinger, F., Kissling, E., Ansorge, J., Hatzfeld, D., Papadimitriou, E., Karakostas, V., Makroploulos, K., Kahle, H.G., Peter, Y., 1999. 3-D crustal structure from local earthquake tomography around the Gulf of Arta (Ionian region, NWGreece). Tectonophysics 304, 201–218.

Husen, S, Kissling, E., Flueh, E., Asch, G., 1999. Accurate hypocentre determination in the seismogenic zone of the subducting Nazca plate in northern Chile using a combined on-/offshore network. Geophys. J. Int. 138: 687-701.

Langer, H., Raffaele, R., Scaltrito, A., Scarfi, L., 2007. Estimation of an optimum Velocity Model in the Peloritani Mountains – Assessment of the variance of model parameters and variability of earthquake locations. Geophys. J. Int. 170, 3, 1151-1164, doi: 10.1111/j.1365-246X.2007.03459.x.

Lentini, F., Catalano, S. & Carbone, S., 2000. Carta geologica della provincia di Messina, Provincia Regionale di Messina. Assessorato Territorio–Servizio geologico, SELCA, Firenze.

Menke, W., and Schaff, D., 2004. Absolute earthquake locations with differential data. Bull. Seism. Soc. Am. 94, 2254 –2264.

Monaco, C., and Tortorici, L., 2000. Active faulting in the Calabrian Arc and eastern Sicily. Journal of Geodynamics 29, 407-424.

Murphy, W., 1995. The geomorphological controls on seismically triggered landslides during the 1908 Straits of Messina earthquake, Southern Italy. Quarterly Journal of Engineering Geology and Hydrogeology 28, 61-74, doi: 10.1144/GSL.QJEGH.1995.028.P1.06.

Neri, G., Barberi, G., Oliva, G., Orecchio, B., 2004. Tectonic stress and seismogenic faulting in the area of the 1908 Messina earthquake, south Italy. Geophys. Res. Lett. 31, 10, doi:10.1029/2004GL019742.

Patacca, E., Sartori, R., and Scandone, P., 1990. Tyrrhenian basin and Appenninic arcs: kinematic relations since late Tortonian times. Mem. Soc. Geol. It., 45, 425-451.

Raffaele, R., Langer, H., Gresta, S., Moia, F., 2006. Tomographic inversion of local earthquake data from the Gioia Tauro basin (south-western Calabria, Italy). Geophys. J. Int. 165, doi: 10.1111/j.1365-246X.2006.02872.x

453 Reasenberg, P. A., and Oppenheimer, D., 1985. FPFIT, FPPLOT and FPPAGE: fortran computer progams for
454 calculating and displaying earthquake fault-plane solutions. Open File Rep., 85-379, 109 pp., U. S. Geol. Surv.,
455 Washington.
456 Scarfì, L., Langer, H., Gresta, S., 2003. High-precision relative locations of two microearthquake clusters in
457 southeastern Sicily, Italy. Bull. seism. Soc. Am. 93**,** 1479–1497.
458 Scarfì, L., Langer, H., Scaltrito, A., 2005. Relocation of microearthquake swarms in the Peloritani mountains –
459 implications on the interpretation of seismotectonic patterns in NE Sicily, Italy. Geophys. J. Int. 163, 225-237, doi:
460 10.1111/j.1365-246X.2005.02720.x.
461 Scarfì, L., Giampiccolo, E., Musumeci, C., Patanè, D., Zhang, H., 2007. New insights on 3D crustal structure in
462 southeastern Sicily (Italy) and tectonic implications from an adaptive mesh seismic tomography. Phys. Earth
463 Planet. Int. 161, 74-85.
464 Selvaggi, G., and Chiarrabba, C., 1995. Seismicity and P-wave velocity image of the Southern Tyrrhenian subduction
465 zone, Geophys. J. Int. 121, 818-826.
466 Stüwe, K., 2002. Geodynamics of the Lithosphere, Springer-Verlag Berlin Heidelberg, pp. 449.
467 Tertulliani, A., Cucci L., 2008. Fenomeni associati al terremoto della Calabria dell'8 settembre 1905. Quaderni di
468 Geofisica., 60.
469 Tortorici, L., Monaco, C., Tansi, C., Cocina, O., 1995. Recent and active tectonics in the Calabrian Arc (southern Italy).
470 Tectonophysics, 243, 37–55.
471 Um, J., and Thurber, C.H., 1987. A fast algorithm for two-point seismic ray tracing. Bull. Seismol. Soc. Am. 77, 972-
472 986.
473 Valensise, G., and Pantosti, D., 1992. A 125 kyr-long geological record of seismic source repeatability: the Messina
474 Straits (southern Italy) and the 1908 earthquake (Ms 71/2). Terra Nova, 4, 472-483.
475 Waldhauser, F., and Ellsworth, W. L., 2000. A double-difference earthquake location algorithm: Method and
476 application to North Hayward Fault, California. Bull. Seism. Soc. Am., 90, 1353-1368.
477 Zhang, H., Thurber, C.H., 2003. Double-difference tomography: The method and its application to the Hayward fault,
478 California. Bull. Seismol. Soc. Am. 93, 1875-1889.
479 Zhang, H., Thurber, C.H., 2005. Adaptive mesh seismic tomography based on tetrahedral and Voronoi diagrams:
480 Application to Parkfield, California. J. Geophys. Res. 110, B04303, doi:10.1029/2004JB003186.
481 Zhao, D., Hasegawa, A., Horiuchi, S., 1992. Tomographic imaging of P and S wave velocity structure beneath
482 northeastern Japan. J. Geophys. Res. 97, 19909-19928.
483

Figure Captions

Fig. 1. Simplified tectonic map (a) and structural sketch map (b) of Sicily and southern Calabria (from Ghisetti, 1992; Lentini et al., 2000). ATG is the abbreviation for Aeolian-Tindari-Giardini faults lineament. Permanent seismic network is also reported: black triangles for Mt. Etna and Aeolian Islands networks and black/white boxes for northeastern Sicily and southern Calabria. Dashed boxes represent the area studied in this paper.

Fig. 2. Map view, N-S and E-W cross sections of the studied area with earthquakes located from 1999 to 2007.

Fig. 3. 3D sketch of P-wave ray paths traced in the minimum 1D model (Langer et al., 2007). Earthquakes and seismic stations are indicated by red circles and blue triangles, respectively.

Fig. 4. Irregular mesh nodes (triangles) for P- (a) and S-waves (b) at the final iteration. At the bottom of the sketches, the projection of the mesh (crosses) and the map of the area (black contour line) are shown.

Fig. 5. DWS value distribution for P waves for the regular inversion grid (a) and irregular inversion mesh (b) at the final iteration (zero values are not shown).

Fig. 6. a) Map of the studied area with the main structural features (from Ghisetti, 1992; Lentini et al., 2000); b) P-wave velocity model for six representative layers resulting from the 3D inversion. Contour lines are at 0.2 km/s intervals. Red circles represent the relocated earthquakes within half the grid size of the slice. The zones with DWS>100 are circumscribed by yellow contour lines.

Fig. 7. Vertical sections through the P-wave velocity model. The traces of sections are reported in the sketch map (A-A", ... F-F"). Contour lines are at 0.4 km/s intervals. White curves contour the zones with DWS>100. Relocated earthquakes, within ± 4 km from the sections, are plotted as red circles.

Fig. 8. P-wave velocity distribution obtained from the characteristic (a) and restoring (b) resolution tests (see text for further details).

Fig. 9. Final event locations in map and vertical sections. The main fault systems are also shown in the map.

Fig. 10. Relative locations of S1 and S2 clusters by using the master-event-technique. Map view (a), vertical cross-sections (b, c) and 3 D sketch (d).

Fig. 11. Focal mechanisms of the major events of the northeastern Sicily and southern Calabria. Their depth are represented together with the fault plane solutions, e. g. Z = 11 (km).

Fig. 12. Topography of the 6.5 km/s P-wave velocity isosurface. Darker colours indicate a greater depth. Contours are at 2.5 km intervals and the numbers indicate the corresponding depths. Relocated earthquakes, above the isosurface, are plotted as red circles.

Fig. 01

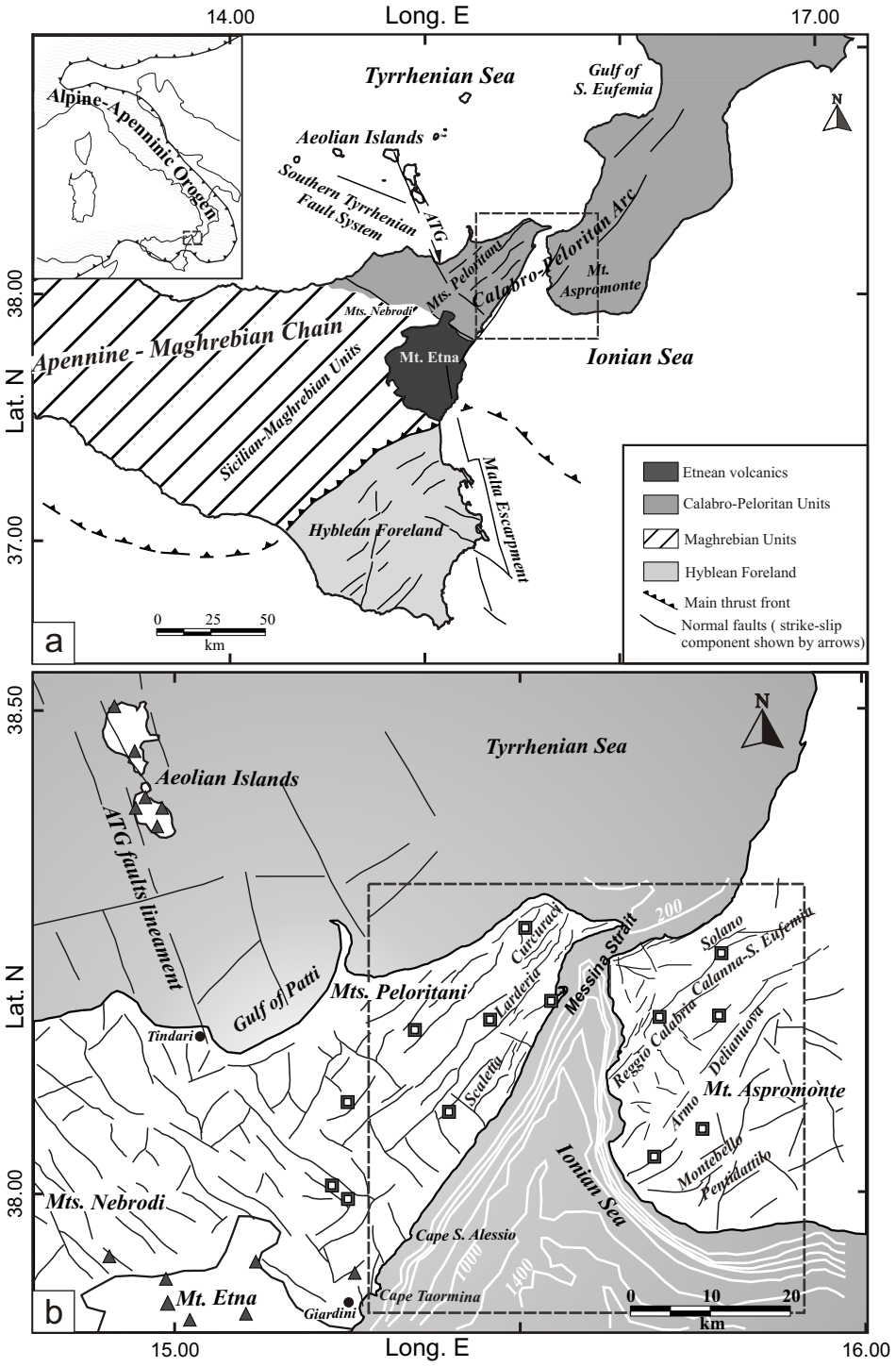
14.00
Long. E
17.00
Tyrrhenian Sea
Gulf of S. Eufemia
Alpine-Apennine Orogen
Aeolian Islands
Southern Tyrrhenian Fault System
ATG
Mts. Peloritani
Calabro-Peloritan Arc
Mt. Aspromonte
Mts. Nebrodi
Apennine - Maghrebian Chain
Mt. Etna
Ionian Sea
Sicilian-Maghrebian Units
Malta Escarpment
Hyblean Foreland
38.00
Lat. N
37.00
0 25 50
km
a
Etnean volcanics
Calabro-Peloritan Units
Maghrebian Units
Hyblean Foreland
Main thrust front
Normal faults (strike-slip component shown by arrows)
38.50
N
Tyrrhenian Sea
Aeolian Islands
ATG faults lineament
Gulf of Patti
Mts. Peloritani
Curcuraci
Messina Strait
200
Solano
Calanna-S. Eufemia
Tindari
Lardería
Reggio Calabria
Dellanuova
Scaletta
Mt. Aspromonte
Armo
Montebello
Pentadattilo
Ionian Sea
Mts. Nebrodi
Cape S. Alessio
1000
1400
Mt. Etna
Giardini
Cape Taormina
0 10 20
km
b
15.00
Long. E
16.00

Fig. 2

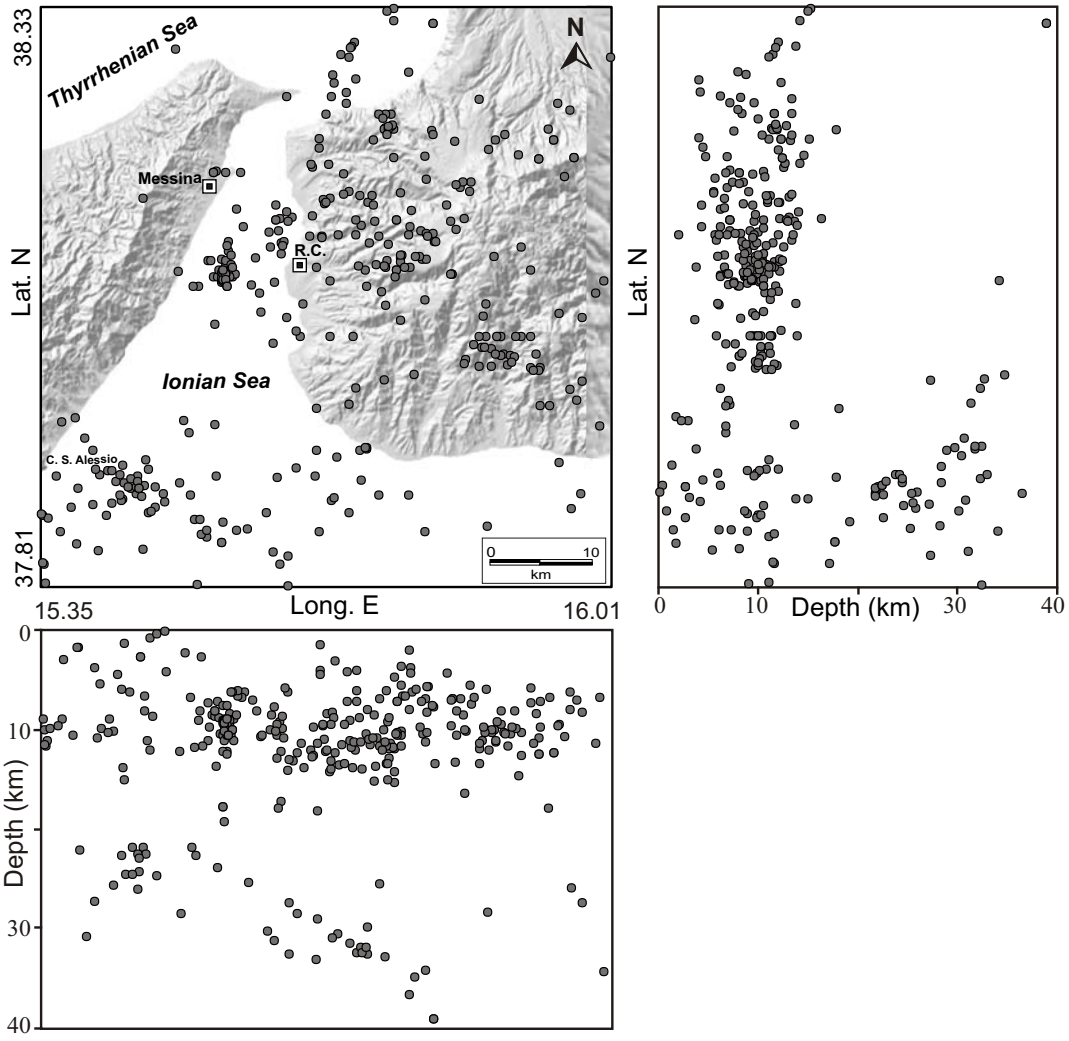
Thyrrhenian Sea
Ionian Sea
Messina
R.C.
C. S. Alessio
N
0
10
km
38.33
37.81
Lat. N
15.35
Long. E
16.01
Lat. N
0
10
Depth (km)
30
40
Depth (km)
0
10
30
40

Fig. 3

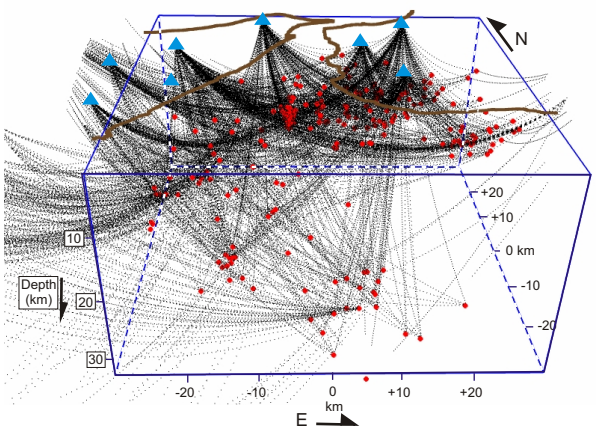

Fig. 4

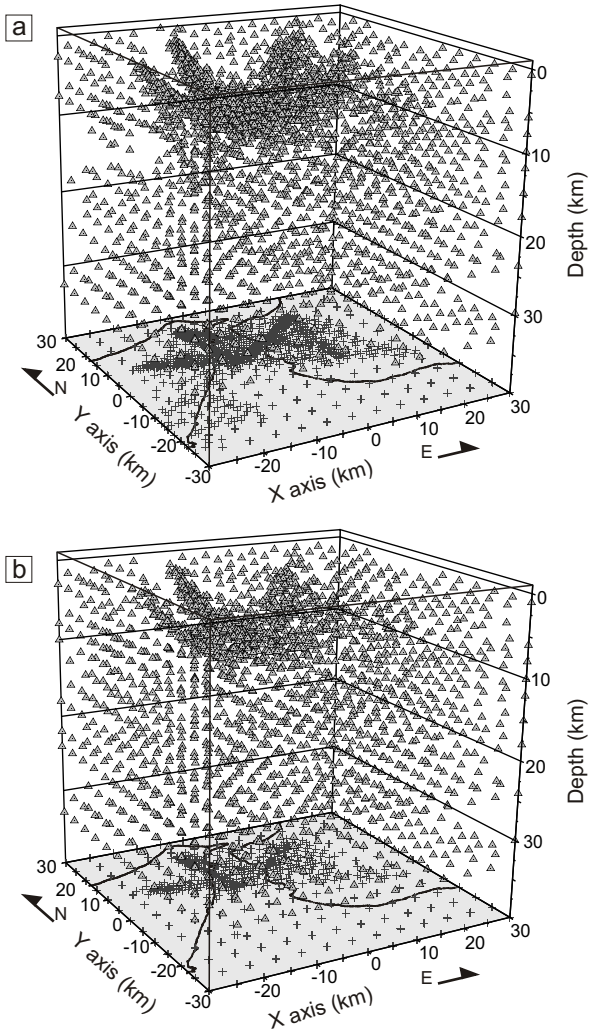

Fig. 5

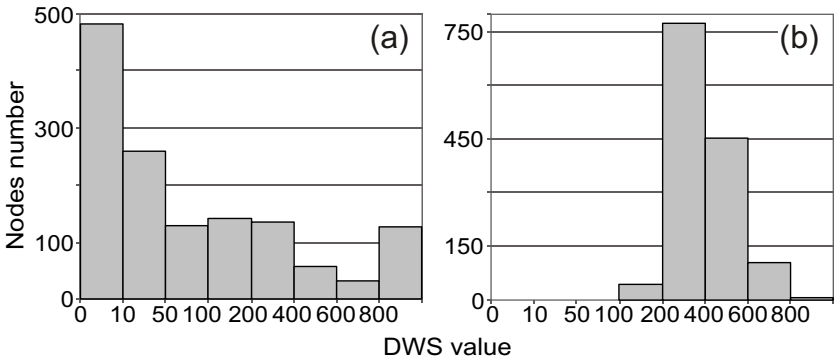
(a)
(b)
Nodes number
500
300
100
0
750
450
150
0
0 10 50 100 200 400 600 800
0 10 50 100 200 400 600 800
DWS value

Fig. 6

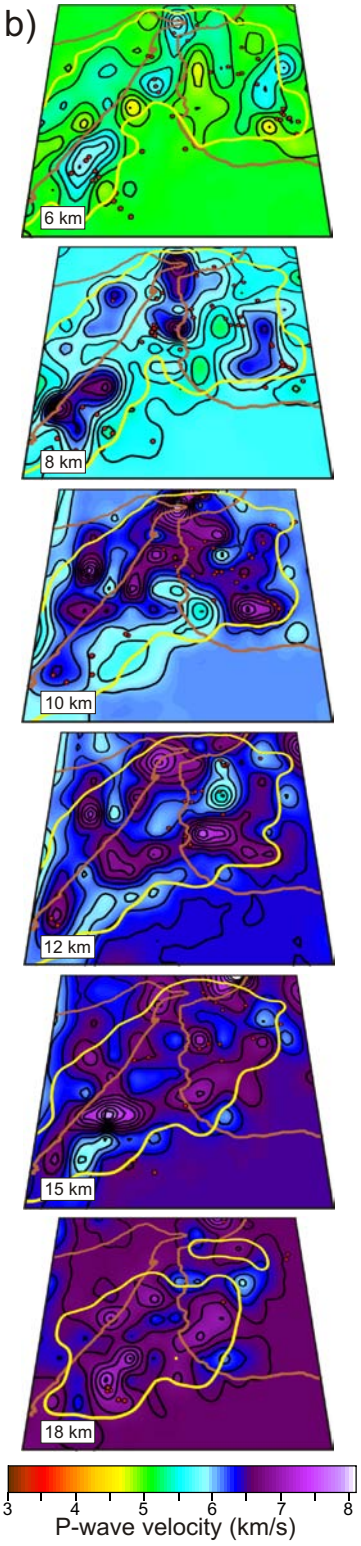
b)
6 km
8 km
10 km
12 km
15 km
18 km
3
4
5
6
7
8
P-wave velocity (km/s)

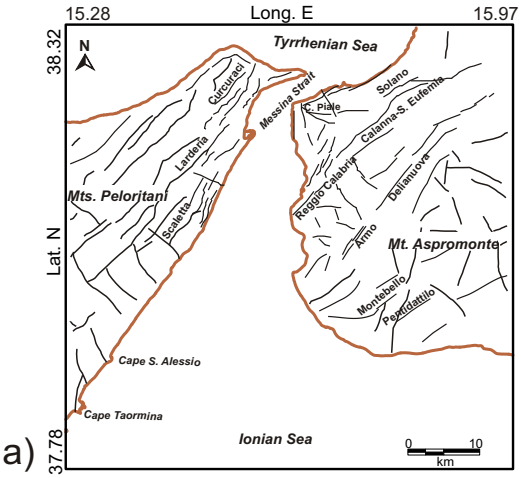
15.28
Long. E
15.97
38.32
Lat. N
37.78
a)
N
Tyrrhenian Sea
Curcuraci
Messina Strait
C. Piale
Solano
Catanina-S. Eufemia
Larderia
Mts. Peloritani
Scaletta
Reggio Calabria
Bellantuono
Ammo
Mt. Aspromonte
Montebello
Pentidattilo
Cape S. Alessio
Cape Taormina
Ionian Sea
0
10
km

Fig. 7

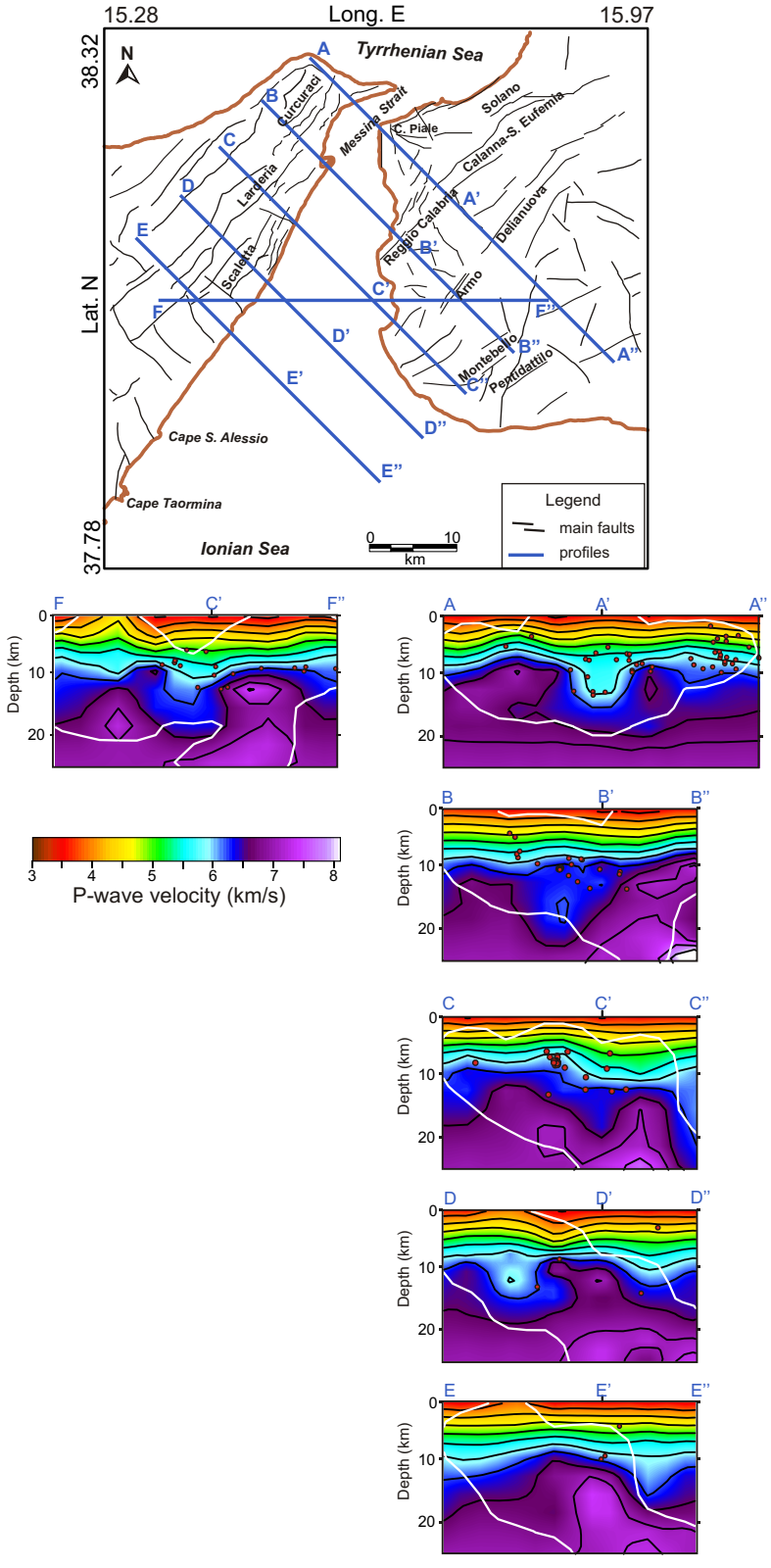
15.28
Long. E
15.97
38.32
Lat. N
37.78
N
Tyrrhenian Sea
Ionian Sea
Curcuraci
Messina Strait
C. Piale
Solano
Calanna-S. Eufemia
Larderia
Scaletta
Reggio Calabria
Armo
Delianuova
Montebello
Peppidattilo
Cape S. Alessio
Cape Taormina
A
A'
A''
B
B'
B''
C
C'
C''
D
D'
D''
E
E'
E''
F
F''
Legend
main faults
profiles
0
10
km
Depth (km)
P-wave velocity (km/s)
3
4
5
6
7
8

Fig. 8

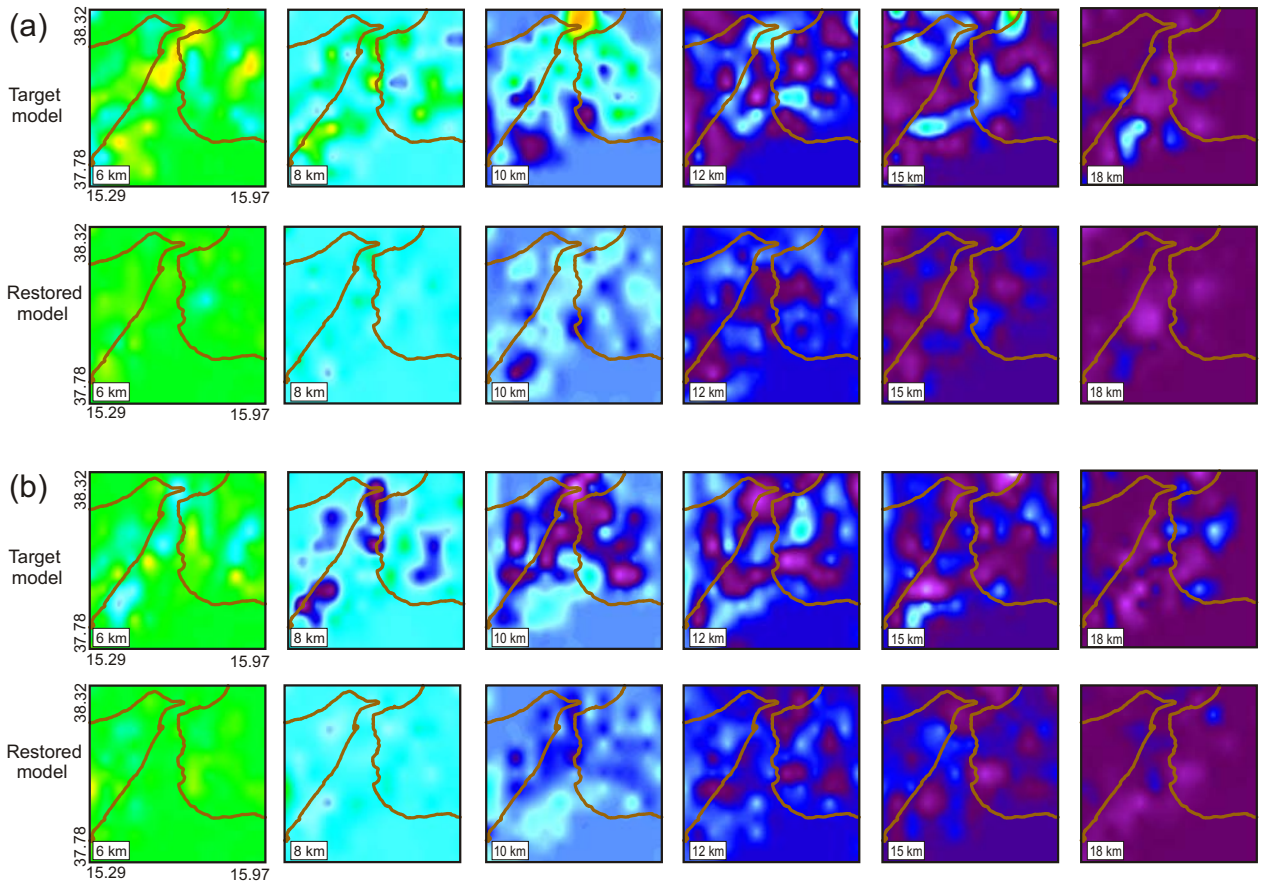
(a)
Target model
Restored model
38.32
37.78
15.29
15.97
6 km
8 km
10 km
12 km
15 km
18 km
(b)
Target model
Restored model
38.32
37.78
15.29
15.97
6 km
8 km
10 km
12 km
15 km
18 km

Fig. 9

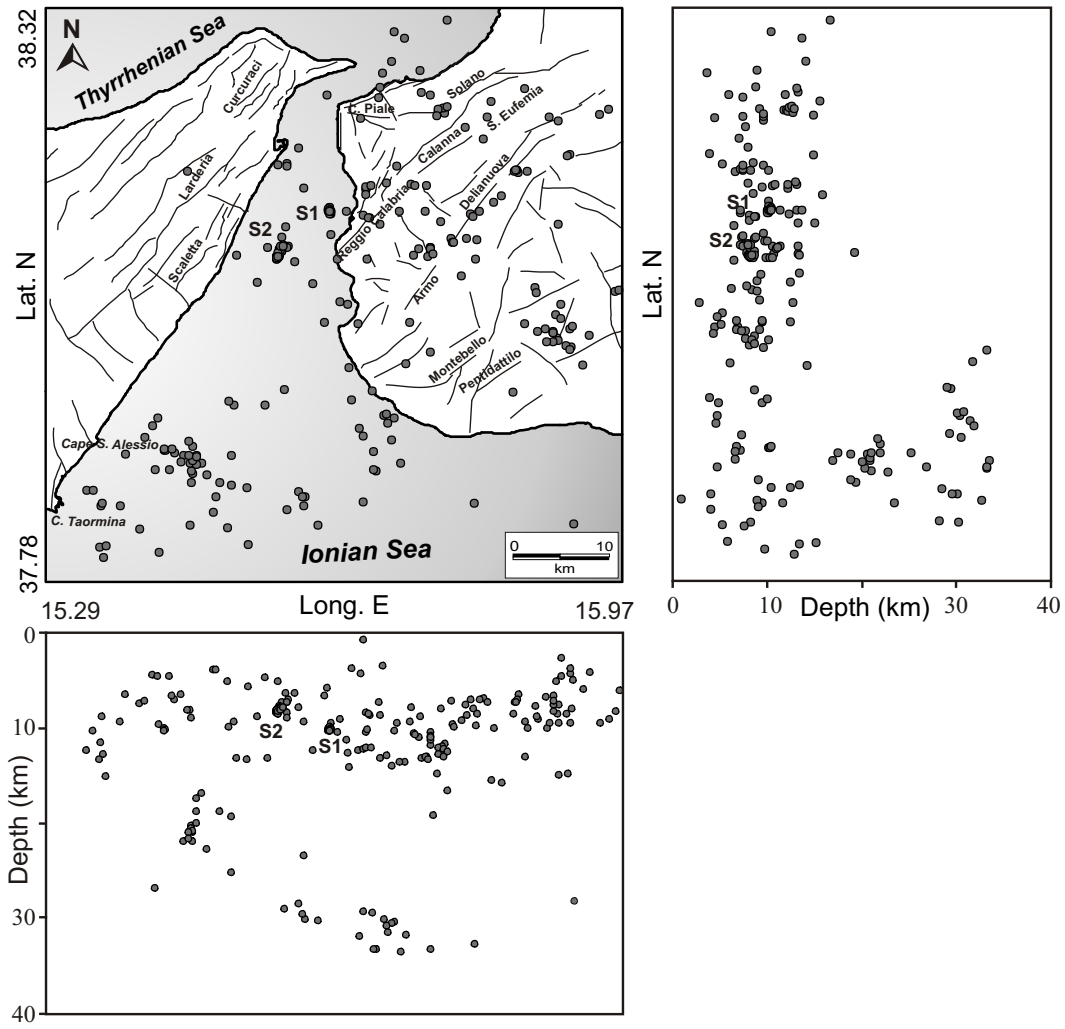
N
Thyrrhenian Sea
Ionian Sea
Cape S. Alessio
C. Taormina
Curcuraci
Capo Piale
Solano
S. Eufemia
Calanna
Pellaniuova
Reggio Calabria
Arino
Montebello
Peppidattilo
Lacleria
Scaletta
S1
S2
0
10
km
38.32
37.78
Lat. N
15.29
Long. E
15.97
Lat. N
Depth (km)
0
10
30
40

Fig. 10

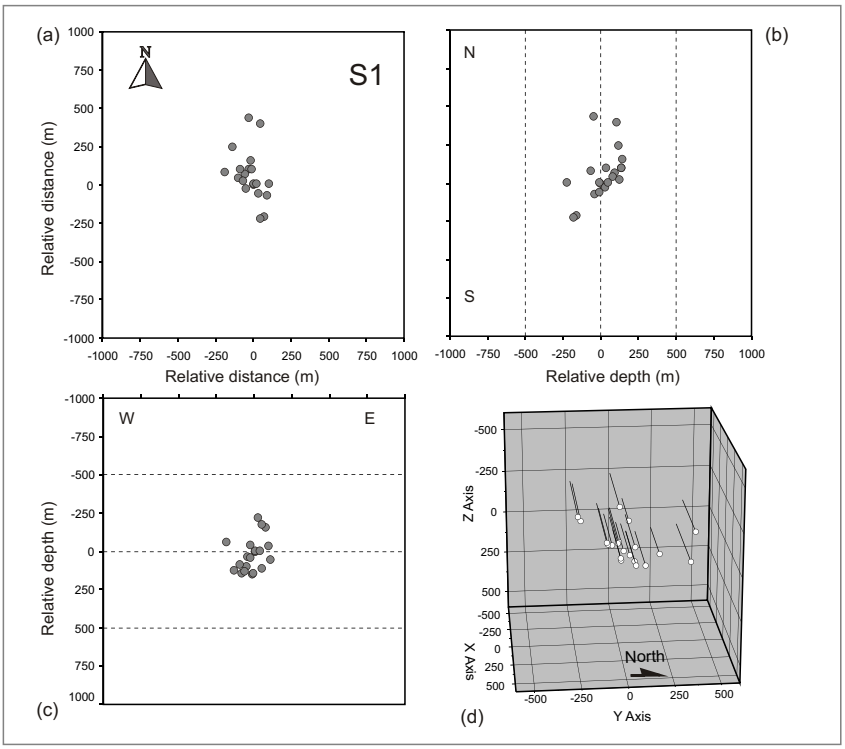
(a)
S1
N
Relative distance (m)
Relative distance (m)
(b)
N
S
Relative depth (m)
W
E
Relative depth (m)
(c)
Z Axis
North
Y Axis
(d)

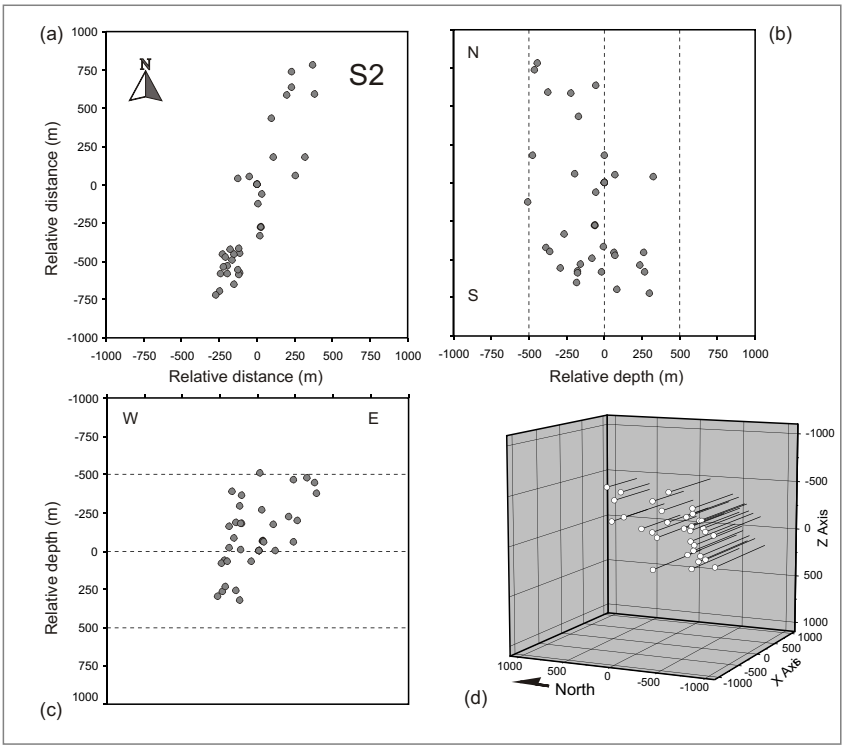
(a)
S2
N
Relative distance (m)
Relative distance (m)
(b)
N
S
Relative depth (m)
W
E
Relative depth (m)
(c)
Z Axis
North
X Axis
(d)

Fig. 11

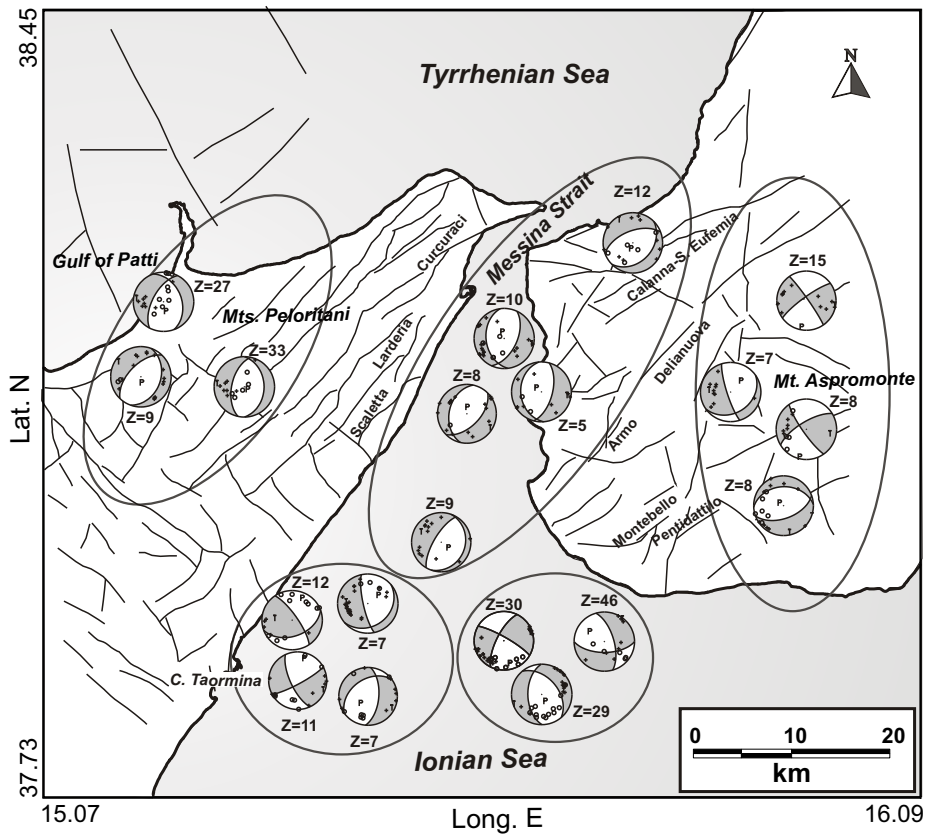
Tyrrhenian Sea
Ionian Sea
Messina Strait
Gulf of Patti
Mts. Peloritani
Mt. Aspromonte
C. Taormina
Curcuraci
Lardena
Scaletta
Calanna-S. Eufemia
Delianuova
Armo
Montebello
Penidattilo
Z=27
Z=33
Z=9
Z=12
Z=10
Z=8
Z=5
Z=9
Z=12
Z=7
Z=11
Z=7
Z=30
Z=46
Z=29
Z=12
Z=15
Z=7
Z=8
Z=8
N
0
10
20
km
38.45
37.73
Lat. N
15.07
16.09
Long. E

Fig. 12

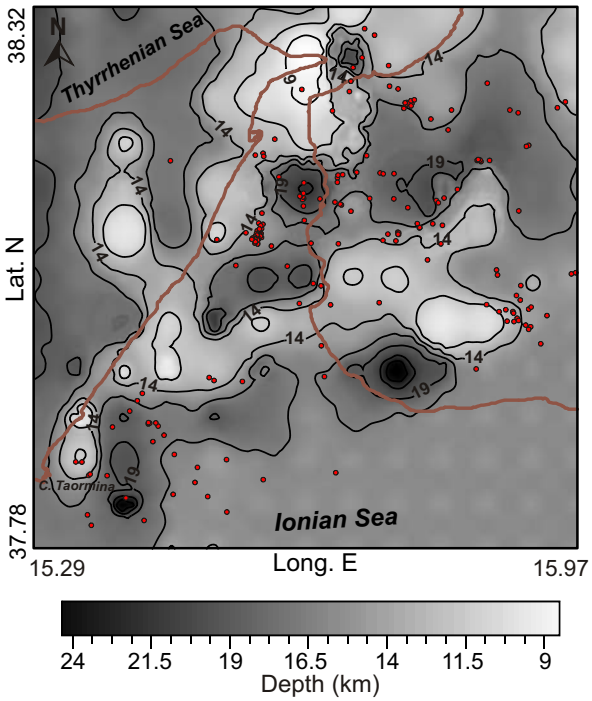
N
Thyrrhenian Sea
Ionian Sea
C. Taormina
38.32
37.78
Lat. N
15.29
Long. E
15.97
24
21.5
19
16.5
14
11.5
9
Depth (km)